Article

Solution H NMR Characterization of the Distal H-Bond Network and the Effective Axial Field in the Resting-State, High-Spin Ferric, Substrate-Bound Complex of Heme Oxygenase from *N. meningitidis*

Yangzhong Liu, Xuhong Zhang, Tadashi Yoshida, and Gerd N. La Mar

J. Am. Chem. Soc., **2005**, 127 (17), 6409-6422• DOI: 10.1021/ja042339h • Publication Date (Web): 06 April 2005

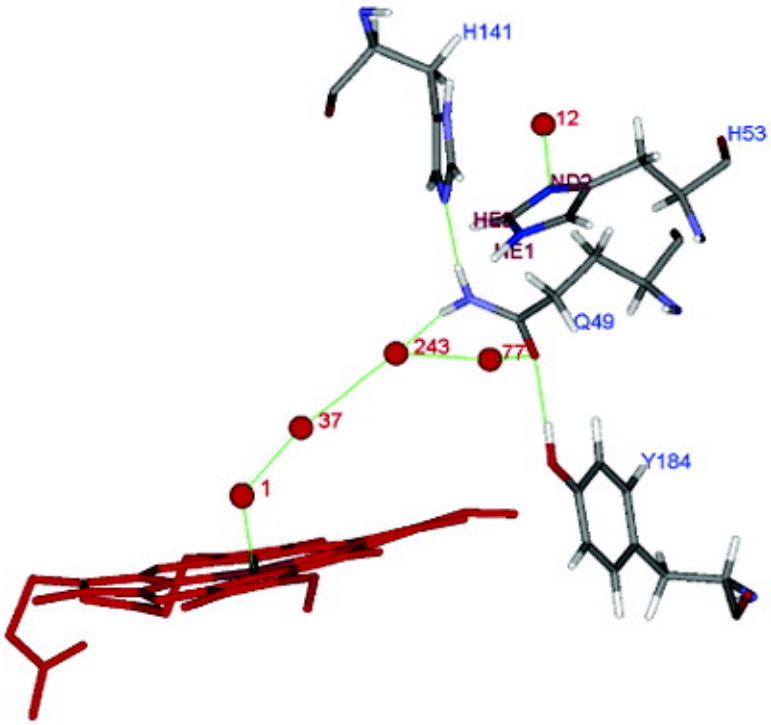

More About This Article

Additional resources and features associated with this article are available within the HTML version:

- Supporting Information
- Links to the 1 articles that cite this article, as of the time of this article download
- Access to high resolution figures
- Links to articles and content related to this article
- Copyright permission to reproduce figures and/or text from this article

J|A|C|S
ARTICLES
Published on Web 04/06/2005

Solution ^{1}H NMR Characterization of the Distal H-Bond Network and the Effective Axial Field in the Resting-State, High-Spin Ferric, Substrate-Bound Complex of Heme Oxygenase from *N. meningitidis*

Yangzhong Liu,[†] Xuhong Zhang,[‡] Tadashi Yoshida,[‡] and Gerd N. La Mar*,[†]

Contribution from the Department of Chemistry, University of California, Davis, California 95616, and Department of Biochemistry, Yamagata University School of Medicine, Yamagata 990-9585, Japan

Received December 20, 2004; E-mail: lamar@chem.ucdavis.edu

Abstract: The solution ^{1}H 1D and 2D NMR spectra of the high-spin ferric, resting-state, substrate-bound complex of heme oxygenase, HO, from the pathological bacterium *N. meningitidis* have been investigated to assess the prospects for definitive assignment of hyperfine shifted and relaxed residue protons and the interpretation of those shifts in terms of the anisotropy and orientation of the paramagnetic susceptibility tensor, χ. Appropriately tailored 1D/2D NMR data, together with analyses of paramagnetic relaxation and a preliminary estimate of the magnetic anisotropy, reveal a χ that is axially anisotropic and oriented along the Fe−His vector. Together with T^{-2} dependence of the shifts, $\Delta\chi_{ax}$ yields a zero-field splitting constant, $D = 9.1$ cm^{-1}, which is expected to serve as a very sensitive probe of H-bond interactions between the iron-ligated water and a series of distal ordered water molecules implicated in the mechanism of HO action. The side chains, Gln49 and His53, involved in the stabilization of catalytically relevant water molecules, were found to exhibit orientations rotated by 180° about the $\beta-\gamma$ bonds in solution relative to those in the crystal. The implication of these reorientations on the details of the distal H-bond network is discussed. The H-bond donor strengths of Gln 49 and His53 were found to respond appropriately to H-bond donor (water) versus H-bond acceptor (cyanide) iron ligands. Very slow NH exchange for the N-terminal portion of the distal helix suggest that an intrinsically "unstable" distal helix may be valid only for the C-terminal portion.

Introduction

Heme oxygenase (HO[1]) is a widely occurring, nonmetal enzyme that converts hemin, [1−5] via two well-characterized intermediates, meso-OH-protoheme and verdoheme, into biliverdin, CO, and iron using either NADPH or a ferredoxin as an electron source.[2−5] In mammals, HO is crucial to iron homeostasis,[6] the production of the antioxidant bilirubin[7] (converted from biliverdin by biliverdin reductase), and the putative neural messenger, CO.[8] Pathogenic bacteria utilize HO to "free" iron from Hb in hosts,[9,10] and plants rely on HO to generate precursors to light-transmitting tetrapyrroles.[11] The different HOs share variable sequence homology[12−14] with the much more extensively studied human HO#1, hHO, and rat HO#1, rHO,[1−5] and crystal structures of human[15,16] and rat[17,18] HO, as well as those from the bacteria *N. meningitidis*, [19,20] HemO, *C. diphtheriae*,[21,22] HmuO, and *P. aeruginosa*,[23] PigA, identify a conserved fold that locates a distal helix placed so close to the

[†] University of California, Davis.
[‡] Yamagata University School of Medicine.

(1) Tenhunen, R.; Marver, H. S.; Schmid, R. *J. Biol. Chem.* **1969**, *244*, 6388−6394.
(2) Yoshida, T.; Migita, C. T. *J. Inorg. Biochem.* **2000**, *82*, 33−41.
(3) Wilks, A. *Antioxid. Redox Signaling* **2002**, *4*, 603−614.
(4) Ortiz de Montellano, P. R.; Auclair, K. In *The Porphryin Handbook*; Kadish, K. M., Smith, K. M., Guilard, R., Eds.; Elsevier Science: San Diego, CA, 2003; Vol. 12, pp 175−202.
(5) Rivera, M.; Zeng, Y. *J. Inorg. Biochem.* **2005**, *99*, 337−354.
(6) Yoshida, T.; Biro, P.; Cohen, T.; Mueller, R. M.; Shibahara, S. *Eur. J. Biochem.* **1988**, *171*, 457−461.
(7) Stocker, R.; Yamamoto, Y.; McDonagh, A. F.; Glazer, A. N.; Ames, B. N. *Science* **1987**, *235*, 1043−1046.
(8) Maines, M. D. *Annu. Rev. Pharm. Toxicol.* **1997**, *37*, 517−554.
(9) Bullen, J. J.; Griffiths, E. *Iron and Infection: Molecular, Physiological and Clinical Aspects*; John Wiley and Sons: New York, 1999; pp 87−213.
(10) Frankenberg-Dinkel, N. *Antioxid. Redox Signaling* **2004**, *6*, 825−834.
(11) Beale, S. I. *Ciba Foundation Symposium* **1994**, *180*, 156−168.
(12) Schmitt, M. P. *J. Bacteriol.* **1997**, *179*, 838−845.
(13) Wilks, A.; Schmitt, M. P. *J. Biol. Chem.* **1998**, *273*, 837−841.
(14) Ratliff, M.; Zhu, M.; Deshmukh, R.; Wilks, A.; Stojiljkovic, I. *J. Bacteriol.* **2001**, *183*, 6394−6403.
(15) Schuller, D. J.; Wilks, A.; Ortiz de Montellano, P. R.; Poulos, T. L. *Nat. Struct. Biol.* **1999**, *6*, 860−867.
(16) Lad, L.; Wang, J.; Li, H.; Friedman, J.; Bhaskar, B.; Ortiz de Montellano, P. R.; Poulos, T. L. *J. Mol. Biol.* **2003**, *330*, 527−538.
(17) Sugishima, M.; Sakamoto, H.; Higashimoto, Y.; Omata, Y.; Hayashi, S.; Noguchi, M.; Fukuyama, K. *J. Biol. Chem.* **2002**, 45086−45090.
(18) Sugishima, M.; Sakamoto, H.; Noguchi, M.; Fukuyama, K. *Biochemistry* **2003**, *42*, 9898−9905.
(19) Schuller, D. J.; Zhu, W.; Stojiljkovic, I.; Wilks, A.; Poulos, T. L. *Biochemistry* **2001**, *40*, 11552−11558.
(20) Friedman, J. M.; Lad, L.; Deshmukh, R.; Li, H. Y.; Wilks, A.; Poulos, T. L. *J. Biol. Chem.* **2003**, *278*, 34654−34659.
(21) Hirotsu, S.; Chu, G. C.; Unno, M.; Lee, D.-S.; Yoshida, T.; Park, S.-Y.; Shiro, Y.; Ikeda-Saito, M. *J. Biol. Chem.* **2004**, *279*, 11937−11947.
(22) Unno, M.; Matsui, T.; Chu, G. C.; Coutoure, M.; Yoshida, T.; Rousseau, D. L.; Olson, J. S.; Ikeda-Saito, M. *J. Biol. Chem.* **2004**, *279*, 21055−21061.
(23) Friedman, J.; Lad, L.; Li, H.; Wilks, A.; Poulos, T. L. *Biochemistry* **2004**, *43*, 5239−5245.

heme surface as to sterically block against attack by FeOOH, all but one meso position, the one cleaved in the reaction. Both functional and spectroscopic studies agree that the reactive form is the ferric hydroperoxy species,[5,24−27] rather than the more thoroughly characterized ferryl species common to heme peroxidase and cytochromes P450.[28] The retardation of the heterolytic O−O bond cleavage and stabilization of the Fe^{3+}-OOH species have been attributed to an arrangement of H-bonded, ordered water molecules in the distal pocket, as defined in crystal structures,[16−22] that serve as variable H-bond donor or acceptor during the reaction and as proton source to the nascent $Fe-O_2^-$ species.

Solution ^{1}H NMR has shown that the HO complexes possess extended H-bond networks that involve some unusually strong H-bonds and that these networks extend from the distal cavity to the enzyme surface opposite the substrate pocket.[29−32] The majority of the ^{1}H NMR studies of the enzyme structure have been carried out on the reasonable model for the unstable, reducedO_2 complex, the cyanide-inhibited substrate complexes,[29,33−36] whose low-spin and favorable relaxation rates allow effective 2D characterization to within 4 Å of the iron.[37,38] The low-spin hydroxy complex has also been investigated by both ^{1}H and ^{13}C NMR.[27,34] The dipolar shifts resulting from the rhombic anisotropy characteristics of His/CN ligated hemin,[38] moreover, provided valuable structural constants for identifying similarities to, and differences from, crystallographic results on other derivatives. In one case, it has been possible to elucidate some structural details of substrate-free or apo-HO with respect to tertiary folding, H-bonding, and the presence of water molecules.[39] To date, however, there has been no report of both solution ^{1}H NMR and crystallographical characterization of the *same* substrate complex of any HO. This is due to the fact that the most common crystal studies are on the high-spin HO−PH−H_2O[15,19,21,23,40] and the ferrous HO−PH−NO[16,17] complexes, both of which are paramagnetic and possess quite unfavorable relaxation characteristics for NMR studies.[38,41,42]

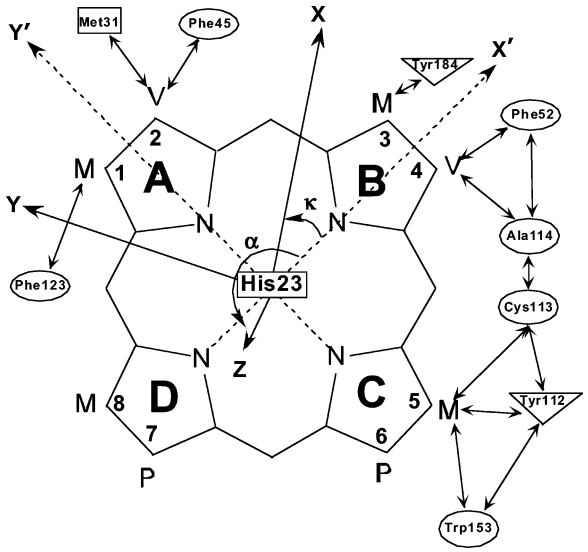

Figure 1. Schematic depiction of the heme and the observed heme contacts. The reference heme-centered coordinate system x', y', z' is related to the magnetic coordinate system x, y, z, where χ is diagonal via the Euler rotation, $\Gamma(\alpha, \beta, \gamma)$, with $(x, y, z) = (x', y', z')\Gamma(\alpha, \beta, \gamma)$; β is the tilt of the major axis from the heme normal, z'; α defines the direction of tilt (angle between the projection of z on the x', y' plane and x'), and $\kappa \approx \alpha + \gamma$ locates the rhombic axis relative to the x' and y' axes. For HemO−PH−H_2O, $\Delta\chi_{rh} \sim 0$, so the angle γ (and hence, κ) is not relevant.

Only the former complex, the resting state substrate complex, is a functionally relevant derivative of the enzyme. However, while both the H_2O and NO complexes will generate broad lines that will severely complicate spectral resolution and 2D NMR characterization,[37] the high-spin HO−PH−H_2O complex exhibits large axial magnetic anisotropy[38,42−47] that results in sizable dipolar shifts such that a significant portion of the active site can be expected to exhibit sufficient resolution for ^{1}H 1D/2D NMR structural characterization. Thus, it is expected that much of the H-bond network should be detectable in HO−PH−H_2O complexes.

The dipolar shifts, like the magnetic anisotropy of high-spin ferric hemoproteins, exhibit highly axial symmetry ($\Delta\chi_{ax} \neq 0$, $\Delta\chi_{rh} \approx 0$), with the major ($z$) axis approximately normal to the heme plane,[38,42,44−47] with

$$\delta_{dip} = (12\pi\mu_o N_A)^{-1} [\Delta\chi_{ax} (3\cos^2\theta' - 1)R^{-3}]\Gamma(\alpha,\beta) \quad (1)$$

where the position of protons in an iron-centered reference coordinate system (with in-plane, x', y' axes as shown in Figure 1) are described by θ' and R. $\Gamma(\alpha,\beta)$ is the Euler transformation that converts the reference coordinates, x', y', z', into the magnetic coordination system, x, y, z, where β and α are the angles that describe the degree of tilt of the major magnetic axis, z, from the heme normal (z'), and the direction of the tilt relative to the x' axis, respectively (Figure 1).[48,49] The closed expressions for the axial anisotropy for high-spin ferric heme

(24) Ortiz de Montellano, P. R. *Acc. Chem. Res.* **1998**, *31*, 543−549.
(25) Davydov, R. M.; Yoshida, T.; Ikeda-Saito, M.; Hoffman, B. M. *J. Am. Chem. Soc.* **1999**, *121*, 10656−10657.
(26) Davydov, R.; Kofman, V.; Fujii, H.; Yoshida, T.; Ikeda-Saito, M.; Hoffman, B. M. *J. Am. Chem. Soc.* **2002**, *124*, 1798−1808.
(27) Rivera, M.; Caignan, G. A. *Anal. Bioanal. Chem.* **2004**, *378*, 1464−1483.
(28) Ortiz de Montellano, P. R. In *Cytochrome P450: Structure, Mechanism, and Biochemistry*, 2nd ed.; Ortiz de Montellano, P. R., Ed.; Plenum Press: New York, 1995; pp 245−304.
(29) Li, Y.; Syvitski, R. T.; Auclair, K.; Wilks, A.; Ortiz de Montellano, P. R.; La Mar, G. N. *J. Biol. Chem.* **2002**, *277*, 33018−33031.
(30) Li, Y.; Syvitski, R. T.; Auclair, K.; Ortiz de Montellano, P. R.; La Mar, G. N. *J. Am. Chem. Soc.* **2003**, *125*, 13392−13403.
(31) Li, Y.; Syvitski, R. T.; Chu, G. C.; Ikeda-Saito, M.; La Mar, G. N. *J. Biol. Chem.* **2003**, *279*, 6651−6663.
(32) Liu, Y.; Zhang, X.; Yoshida, T.; La Mar, G. N. *Biochemistry* **2004**, *43*, 10112−10126.
(33) Syvitski, R. T.; Li, Y.; Auclair, K.; Ortiz de Montellano, P. R.; La Mar, G. N. *J. Am. Chem. Soc.* **2002**, *124*, 14296−14297.
(34) Caignan, G. A.; Deshmukh, R.; Wilks, A.; Zeng, Y.; Huang, H.-w.; Moenne-Loccoz, P.; Bunce, R. A.; Eastman, M. A.; Rivera, M. *J. Am. Chem. Soc.* **2002**, *124*, 14879−14892.
(35) Fujii, H.; Zhang, X.; Yoshida, T. *J. Am. Chem. Soc.* **2004**, *126*, 4466−4467.
(36) Zeng, Y.; Deshmukh, R.; Caignan, G. A.; Bunce, R. A.; Rivera, M.; Wilks, A. *Biochemistry* **2004**, *43*, 5222−5238.
(37) La Mar, G. N.; de Ropp, J. S. *Biol. Magn. Reson.* **1993**, *18*, 1−79.
(38) La Mar, G. N.; Satterlee, J. D.; de Ropp, J. S. In *The Porphyrin Handbook*; Kadish, K. M., Smith, K. M., Guilard, R., Eds.; Academic Press: San Diego, CA, 2000; Vol. 5, pp 185−298.
(39) Li, Y.; Syvitski, R. T.; Auclair, K.; Ortiz de Montellano, P. R.; La Mar, G. N. *J. Biol. Chem.* **2003**, *279*, 10195−10205.
(40) Sugishima, M.; Omata, Y.; Kakuta, Y.; Sakamoto, H.; Noguchi, M.; Fukuyama, K. *FEBS Lett.* **2000**, *471*, 61−66.
(41) Banci, L. *Biol. Magn. Reson.* **1993**, *12*, 79−111.
(42) Bertini, I.; Luchinat, C. *Coord. Chem. Rev.* **1996**, *150*, 1−296.
(43) Brackett, G. C.; Richards, D. L.; Caughey, W. S. *J. Chem. Phys.* **1971**, *54*, 4383−4401.
(44) Kao, Y.-H.; Lecomte, J. T. J. *J. Am. Chem. Soc.* **1993**, *115*, 9754−9762.
(45) Clark, K.; Dugad, L. B.; Bartsch, R. G.; Cusanovich, M. A.; La Mar, G. N. *J. Am. Chem. Soc.* **1996**, *118*, 4654−4664.
(46) Déméné, H.; Tsan, P.; Gans, P.; Marion, D. *J. Phys. Chem. B* **2000**, *104*, 2559−2569.
(47) Asokan, A.; de Ropp, J. S.; Newmyer, S. L.; Ortiz de Montellano, P. R. *J. Am. Chem. Soc.* **2001**, *123*, 4243−4254.
(48) Williams, G.; Clayden, N. J.; Moore, G. R.; Williams, R. J. P. *J. Mol. Biol.* **1985**, *183*, 447−460.
(49) Emerson, S. D.; La Mar, G. N. *Biochemistry* **1990**, *29*, 1556−1566.

is given by[50]

$$\Delta\chi_{ax} = \mu_o N_A B^2 \left[\frac{2(g_{||}^2 + g_{\perp}^2)}{kT} - \frac{14D}{5k^2T^2}\left(g_{||}^2 + \frac{1}{2}g_{\perp}^2\right)\right] \quad (2)$$

where $g_\perp$ and $g_{||}$ are the spectroscopic splitting factors parallel and normal, respectively, to the unique axis, *z*, *B* is the Bohr magneton, and *D* is the zero-field splitting constant. It is noted that anisotropy due to the *g*-tensor leads to strictly T^{-1} behavior for δ_{dip} (first term in eq 2), while zero-field splitting leads to strictly T^{-2} behavior (second term in eq 2). The value of the zero-field splitting constant, *D*, in high-spin ferric hemes is well understood,[43,44,46,47,51] with a relatively large magnitude 5−15 cm^{-1} that directly monitors effective axial field strength. Since the ligated water interacts (H-bonds) primarily with the nonligated, ordered "catalytic" water molecules in the distal pocket of HO−PH−H_2O complexes,[15,19,23,40] the measurement of *D* could provide a sensitive probe of perturbations of the distal H-bond network that orders these "catalytic" water molecules in the distal cavity. Variable H-bonding interactions of the axial water in different HO complexes are evident in the variable p*K* values in the conversion of HO−PH−H_2O into HO−PH−OH.[52−54]

To both explore the effectiveness of homonuclear 1D/2D approaches to the HO−PH−H_2O complex for assigning resonances and defining structure and assess the utility of the resulting dipolar shifts in elucidating in detail the magnetic/electronic properties of the heme iron as related to axial interactions, we report here on such studies of the HO complex of *N. meningitidis*, HemO−PH−H_2O. We demonstrate that appropriately tailored 1D/2D NMR is capable of providing a wealth of structural information[37,45,47] relative to both H-bonding interaction with the HO matrix as well as between the ligated and unligated water molecules.

Experimental Section

Enzyme Preparation: The apo-HemO samples used in this study are the same as those described in detail previously.[32] Stoichiometric amounts of protohemin, PH (Figure 1), dissolved in 0.1 M KOH in ^1H_2O were added to apo-HemO in phosphate buffered (100 mM, pH 7.0). The substrate complex was purified by column chromatography on Sephadex G25 and yielded samples ~3 mM in HemO−PH−H_2O at pH 7.0. Samples in ^1H_2O were converted to ^2H_2O by column chromatography.[55]

NMR Spectroscopy: ^1H NMR data were collected on Bruker AVANCE 500 and 600 spectrometers operating at 500 and 600 MHz, respectively. Reference spectra at 500 MHz were collected in ^1H_2O and ^2H_2O over the temperature range 10−35 °C at repetition rates of 1 s^{-1} (14 ppm bandwidth) and 5 s^{-1} (200 ppm bandwidth) using a standard one-pulse sequence, as well as with 3:9:19 "soft" pulse detection[56] with and without saturation of the water solvent signal. WEFT spectra[57] were recorded to emphasize strongly relaxed resonances (repetition rate 10 s^{-1}, relaxation delay 5 to 50 ms). Steady-state NOE difference spectra were generated from the 3:9:19 spectra with on-resonance and off-resonance saturation of the desired signals. Chemical shifts are referenced to 2,2-dimethyl-2-silapentane-5-sulfonate (DSS) through the water resonance calibrated at each temperature. Nonselective T_1's were estimated in both ^1H_2O and ^2H_2O at 20, 25, and 30 °C from the null point of a standard inversion−recovery pulse sequence. The distance of a given proton, H_i, from the iron, R_{H_i}, was estimated from the relation $R_{H_i} = R^*_{Fe}[T_1^*/T_{1i}]^{1/6}$, which, using the heme methyl for H* (R^*_{Fe} = 6.1 Å and T_1^* = 6 ms) as reference, yields

$$R_{H_i} = 4.54T_{1i}^{0.1667} \quad (3)$$

600 MHz NOESY[58] spectra (mixing time, 40 ms; 15−35 °C) and 500 MHz Clean-TOCSY (to suppress ROESY response[59]) spectra (25, 35 °C, spin lock 15−40 ms) using MLEV-17[60] were recorded over a bandwidth of 15 kHz (NOESY) and 12 kHz (TOCSY) with recycle rates of 1−5 s^{-1}, using 512 t1 blocks of 128 or 256 scans each consisting of 2048 t2 points. 2D data sets were processed using Bruker XWIN software on a Silicon Graphics Indigo workstation and consisted of 30°- or 45°-sine-squared-bell-apodization in both dimensions and zero-filling to 2048 × 2048 data points prior to Fourier transformation.

Magnetic Axes Determination: The location of the magnetic axes were determined by finding the Euler rotation angles, $\Gamma(\alpha,\beta,\gamma)$, that rotate the crystal-structure-based, iron-centered reference coordinate system, *x*′, *y*′, *z*′, into the magnetic coordinate system, *x*, *y*, *z*, where the paramagnetic susceptibility tensor, χ, is diagonal where α, β, γ are the three Euler angles.[49] The angle β dictates the tilt of the major magnetic axis, *z*, from the heme normal *z*′, α reflects the direction of this tilt and is defined as the angle between the projection of the *z* axis on the heme plane and the *x*′ axis (Figure 1), and $\kappa \approx \alpha + \gamma$ is the angle between the projection of the *x*, *y* axes onto the heme plane and locates the rhombic axes (Figure 1). In the present case, we consider the tensor to be axially symmetric, so that $\Delta\chi_{rh} = 0$, and γ becomes irrelevant. The magnetic axes were determined by a least-squares search for the minimum in the error function, *F*/*n*:[29,38,48,61]

$$F/n = \sum_{i=1}^{n} |\delta_{dip}(\text{obsd}) - \delta_{dip}(\text{calcd})|^2 \quad (4)$$

where the calculated dipolar shift in the reference coordinate system, *x*′, *y*′, *z*′ or *R*, θ' Ω', is given by eq 1 with $\Delta\chi_{ax}$ and $\Delta\chi_{rh}$ as the axial and rhombic anisotropies of the diagonal paramagnetic susceptibility tensor. The observed dipolar shift, δ_{dip}(obsd), is given by

$$\delta_{dip}(\text{obsd}) = \delta_{DSS}(\text{obsd}) - \delta_{DSS}(\text{dia}) \quad (5)$$

where δ_{DSS}(obsd) and δ_{DSS}(dia) are the chemical shifts, in ppm, referenced to DSS, for the paramagnetic HemO−PH−H_2O complex and an isostructural diamagnetic complex, respectively. In the absence of an experimental δ_{DSS}(dia) for the latter, it may be reliably estimated[31,62] from the available molecular structure[19,20] and available computer programs[63,64] as described previously for HemO−PH−CN.[32]

Results

The strongly hyperfine shifted portions of the ^1H NMR spectrum of HemO−PH−H_2O in ^1H_2O at 25 °C are illustrated

(50) Kurland, R. J.; McGarvey, B. R. *J. Magn. Reson.* **1970**, *2*, 286−301.
(51) Rajarathnam, K.; La Mar, G. N.; Chiu, M. L.; Sligar, S. G.; Singh, J. P.; Smith, K. M. *J. Am. Chem. Soc.* **1991**, *113*, 7886−7892.
(52) Takahashi, S.; Wang, J.; Rousseau, D. L.; Ishikawa, K.; Yoshida, T.; Host, J. R.; Ikeda-Saito, M. *J. Biol. Chem.* **1994**, *269*, 1010−1014.
(53) Sun, J.; Wilks, A.; Ortiz de Montellano, P. R.; Loehr, T. M. *Biochemistry* **1993**, *32*, 14151−14157.
(54) Chu, G. C.; Tomita, T.; Sönnichsen, F. D.; Yoshida, T.; Ikeda-Saito, M. *J. Biol. Chem.* **1999**, *274*, 24490−24496.
(55) Johnston, P. D.; Figueroa, N.; Redfield, A. G. *Proc. Natl. Acad. Sci. U.S.A.* **1979**, *76*, 3130−3134.
(56) Piotto, M.; Sandek, V.; Sklenar, V. *J. Biomol. NMR* **1992**, *2*, 661−666.
(57) Gupta, R. K. *J. Magn. Reson.* **1976**, *24*, 461−465.
(58) Jeener, J.; Meier, B. H.; Bachmann, P.; Ernst, R. R. *J. Chem. Phys.* **1979**, *71*, 4546−4553.
(59) Griesinger, C.; Otting, G.; Wüthrich, K.; Ernst, R. R. *J. Am. Chem. Soc.* **1988**, *110*, 7870−7872.
(60) Bax, A.; Davis, D. G. *J. Magn. Reson.* **1985**, *65*, 355−360.
(61) Emerson, S. D.; La Mar, G. N. *Biochemistry* **1990**, *29*, 1545−1555.
(62) La Mar, G. N.; Asokan, A.; Espiritu, B.; Yeh, D. C.; Auclair, K.; Ortiz de Montellano, P. R. *J. Biol. Chem.* **2001**, *276*, 15676−15687.
(63) Neal, S.; Nip, A. M.; Zhang, H.; Wishart, D. S. *J. Biomol. NMR* **2003**, *26*, 215−240.
(64) Cross, K. J.; Wright, P. E. *J. Magn. Reson.* **1985**, *64*, 220−231.

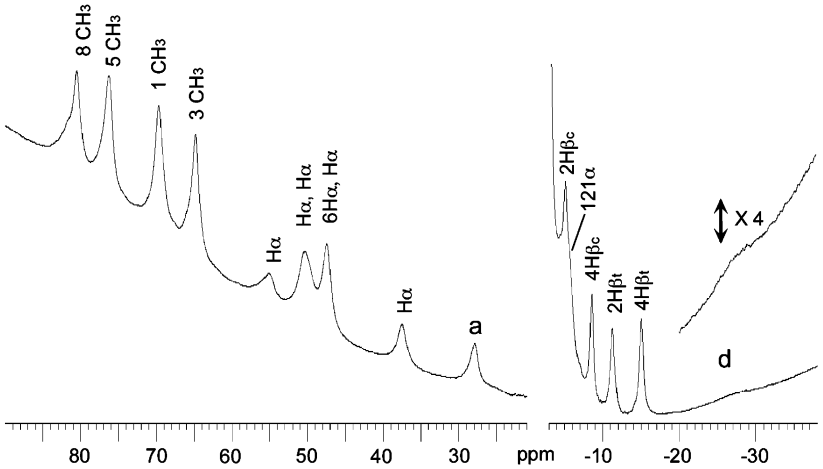

Figure 2. Resolved portions of the ^{1}H NMR spectrum of HemO−PH−H_2O in ^1H_2O, 50 mM in phosphate, pH 7.0 at 25 °C. Peaks are labeled as definitively assigned herein. Peaks assigned only indirectly based on dipolar shift/relaxation prediction are shown by letters.

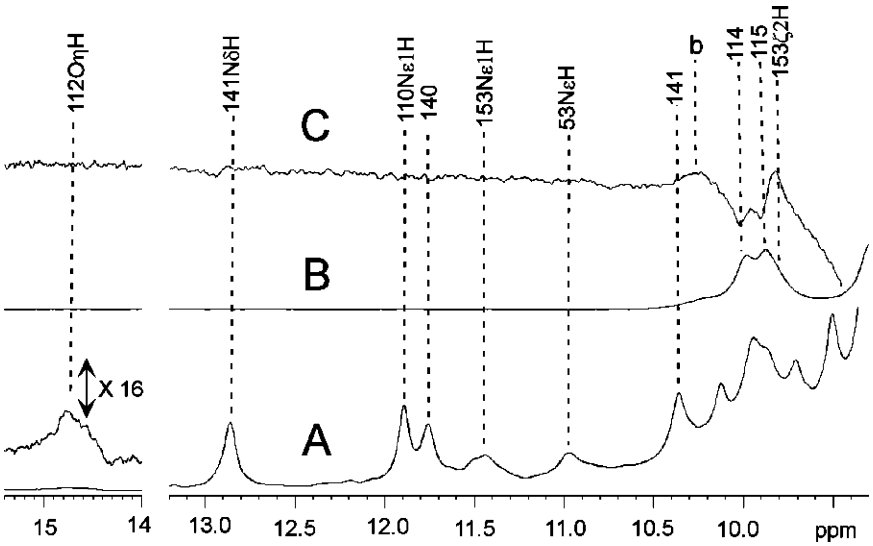

Figure 3. The 600 MHz ^{1}H NMR spectrum of HemO−PH−H_2O for the resolved labile protons to the low-field side of the diamagnetic envelope in ^1H_2O, 50 mM in phosphate at 25 °C; (A) 3:9:19 spectrum[56] in ^1H_2O without saturation of the solvent signal; (B) after 1 month in ^2H_2O; and (C) shows a partially relaxed ^{1}H NMR spectrum (repetition rate 2 s^{-1}, relaxation delay 50 ms) of the four-peak composite peak that allows differentiation of the individual shift/relaxation properties. Peaks are labeled by residue number and position; peptide NH's are labeled solely by number.

in Figure 2. T_1 determination reveals values of ∼6 ms for the low-field methyls and 15, 25 ms for the obvious, upfield vinyl $H_{\beta t}$ and $H_{\beta c}$ peaks, respectively; signals labeled H_α are heme propionate and/or vinyl C_αH's ($T_1 \sim 4$ ms). The low-field single proton peak a and a much broader upfield resonance (labeled d) of indeterminate intensity exhibit T_1's of ∼2 ms and <1 ms, respectively. The resolved, low-field portion of a "3:9:19" ^{1}H NMR spectrum[56] in ^1H_2O is expanded in Figure 3A, and the resolved portions on the upfield edge of the diamagnetic envelope are displayed in Figure 4A,B,B′. Peaks are labeled as assigned on the basis of definitive 1D/2D NMR constraints.

Several weeks after replacement of ^1H_2O with ^2H_2O, intensity is lost for many, but not all, labile protons, leaving two prominent composites near 9.8 and 10.3 ppm (Figure 3B), of which all but one (Trp153 $C_{\epsilon 2}$H) are very slowly exchanging labile protons. The individual shifts and relaxation properties are readily differentiated in a partially relaxed spectrum (relaxation delay 50 ms) in a T_1 determination (Figure 3C) that reveals that labile proton peak b at 10.3 ppm exhibits $T_1 \approx 20$ ms; peak b does not exhibit detectable TOCSY/NOESY cross-peaks. While intensity loss in the crowded 7−9 ppm window is obvious in the comparison of the spectra in ^1H_2O and ^2H_2O (not shown), significant labile proton intensity is retained over several months and the distribution of the intensity is spatially selective since several helical fragments allow ready detection of N_i-N_{i+1} cross-peaks after several months in ^2H_2O (see below).

Assignment Protocols: Effective paramagnetic relaxation results in heme methyl T_1's of ∼6 ms, which lead to a correlation[38,41,42] between R_{Fe-i} and T_{1i} for proton i as given by eq 3. The plot of this equation is illustrated in the line in Figure 5. Thus the immediate vicinity of the heme iron, $R_i < 8$ Å, will not likely participate in 2D experiments. In view of this expected relaxation, our assignments will initially focus on standard, sequence-specific assignment[65] using NOESY connectivities among TOCSY-detected backbone spin systems in ^1H_2O solution for resonance relatively weakly influenced by relaxation. Since it has been shown in the cyanide complex[32] that numerous residues of interest exhibit very slow peptide NH exchange with solvent (half-lives > 1 month), similar sequence-specific

(65) Wüthrich, K. *NMR of Proteins and Nucleic Acids*; Wiley & Sons: New York, 1986.

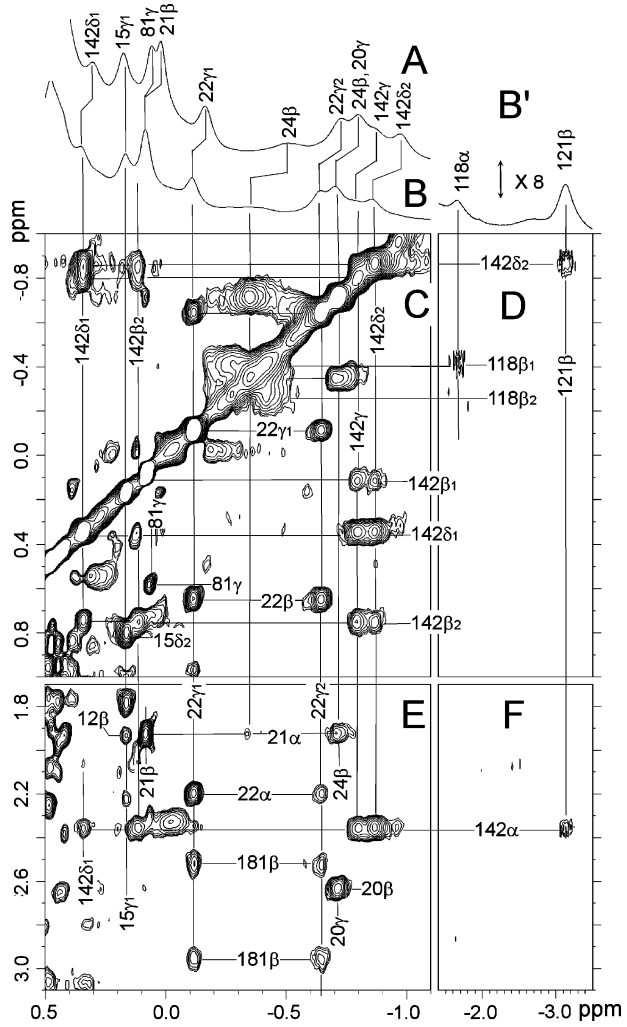

Figure 4. Resolved upfield portion of the 600 MHz ^{1}H NMR spectra at 18 °C (A) and at 25 °C (B, B′) and upfield portions of the NOESY (mixing time 40 ms) spectra (C−F), illustrating the intra-residue cross-peaks for Thr20 and Ala21 (E), Val22 and Leu142 (C, E), Asn118 (C, D), and Asp24 (C), as well as key inter-residue cross-peaks within the residue pair Ala121/Leu142 (D, F), Asn118/Ala121 (D), Ala21/Asp24 (E), and Val22/Phe181 (E). The horizontal shift scale for (B′), (C), (E), and (F) are compressed by $^1/_3$, relative to those in (A), (B), (C), and (E), and the vertical scale in (B′) is expanded by 8 relative to that in (B). Peaks are labeled as defined in Figure 3.

assignments are then pursued in ^2H_2O, where the loss of many NH's of no further interest results in remarkable spectral resolution in the crucial 5−10 ppm window. With these sequence-specifically assigned residues, several of which exhibit significant δ_{dip}, a set of "preliminary" magnetic axes are generated by a one-parameter search for $\Delta\chi$, assuming that the anisotropy is axial ($\Delta\chi_{rh} = 0$), and is oriented along the heme normal (i.e., $\alpha = 0$, $\beta = 0$, in eq 1 so $\Gamma(\alpha, \beta) = 1$).

With the available assignments described above, we turn to the interpretation of three key pieces of information for active site residues; the T_1 of a peak of interest, which identifies the R_{H_i} via eq 3, the δ_{dip} (eq 1) predicted by these preliminary magnetic axes, and the crystal coordinates of the same HemO−PH−H_2O complex[19] to assign more strongly relaxed proton signals. The complete set of assigned residues will then be used for both five- and three-parameter searches for a determination of "robust" anisotropies and orientation of χ. In all cases, the repetition and mixing times for 2D experiments are tailored to the expected relaxation,[37] and extensive use is made of variable temperature data to improve resolution, establish unique connectivities even within the crowded spectral regions, and to provide information on the intrinsic temperature dependence of δ_{dip}. The adherence to primarily T^{-1} or T^{-2} dependence (whichever yields intercepts at $T^{-1} = 0$ that agree with expectations for a diamagnetic analog) will allow distinction between $\Delta\chi$ arising from *g*-tensor anisotropy (first term in eq 2) and zero-field splitting (second term in eq 2).

Sequence-Specific Assignments in ^1H_2O: Numerous labile protons are resolved in primarily the region downfield of ∼10 ppm, for which sufficient N_i-N_{i+1}, α_i-N_{i+1}, $\alpha_i-\beta_{i+1}$, α_i-N_{i+3}, and/or $\alpha_i-\beta_{i+3}$ connections are observed (Figure 6) among TOCSY-connected residues (not shown; see Supporting Information) to identify the fragment Ala_i-$(N\alpha)_{i+1}$-Z_{i+2}-Leu_{i+3}-Ala_{i+4}, (Z = long chain), where α_{i+2} and N_{i+2} exhibit NOESY connections (Figure 6E) to an obvious His $C_\delta H$ at 5.3 ppm that is TOCSY-connected (at $\tau_m = 40$ ms) to the $C_\epsilon H$ at 7.14 ppm. The relevant sequential dipolar contacts are summarized in Figure 7. The strong low-field bias of N_{i+1} and N_{i+2} (Figure 6J), as well as NOESY contacts of this fragment, are essentially the same as previously described for HemO−PH−CN[32] and identify Ala139-Ala143, key parts of the characteristic H-bonding network. The non-peptide labile proton at 12.8 ppm exhibits NOESY contact to only the $C_\epsilon H$ of His141, identifying the former as the His141 $N_{\delta 1}H$ ($\delta 1$ position defined in crystal).[15] The complete Leu142 exhibits substantial upfield δ_{dip}, as shown in Figure 4A and 4B, and moderate relaxation, $T_1(C_{\delta 2}H_3)$ ∼90 ms, $T_1(C_\gamma H)$ ∼120 ms, indicative of R_{Fe} ∼9.5 and 10 Å, respectively, in agreement with crystallographic values,[15] 9.9 and 10.5 Å, respectively. Two additional fragments are AMX_m-Ala_{m+1}, with AMX in contact with a 3-spin ring, and Ala_m-Val_{m+1} (see Figure 6). The former must arise from Phe11, Ala12 (Figure 6L), and the latter can correspond only to Ala55-Val56 or Ala80-Val81 and will be shown to arise from the latter (see below). Inadequate resolution precludes definitive assignments of other hyperfine-shifted spin systems in ^1H_2O. The shift and relaxation data for assigned residues with at least one proton with $|\delta_{dip}(obsd)| > 1$ ppm, as well as important residues in the distal H-bond network, are listed in Table 1; other assigned residues are provided in Supporting Information (Table S1).

Sequence-Specific Assignments in ^2H_2O: Three key helical fragments, including their very slowly exchanging NH's, are more readily characterized in ^2H_2O by NOESY data shown in Figure 8. The components of two fragments exhibit only small δ_{dip} and weak paramagnetic relaxation and consists of Ala_j-AMX_{j+1}-Ala_{j+2}-AMX_{j+3}-AMX_{j+4}- and Val_k-Val_{k+1} (shown in Figure 8G), with AMX_{j+1} and AMX_{j+2} exhibiting NOESY cross-peaks to aromatic ring protons. The sequence independently identifies these fragments as Ala180-Phe181-Ala182-Phe183-Tyr184 and Val186-Val187, as confirmed by the α_{183}-N_{186} and α_{184}-β_{187} NOESY cross-peaks (Figure 7). It was not possible to detect the Tyr184 ring by its expected NOESY cross-peaks for the C_βH's (but is observed by its contact to the 4-vinyl; see below), and only one ring proton (C_δH's; Figure 8I) is detected for Phe181 (due to expected severe relaxation). The assignments are confirmed by the observed (as expected) NOESY cross-peaks between the rings of Trp110 and Phe183 (not shown). The third fragment exhibits several backbone protons with significant low-field bias and significant temper-

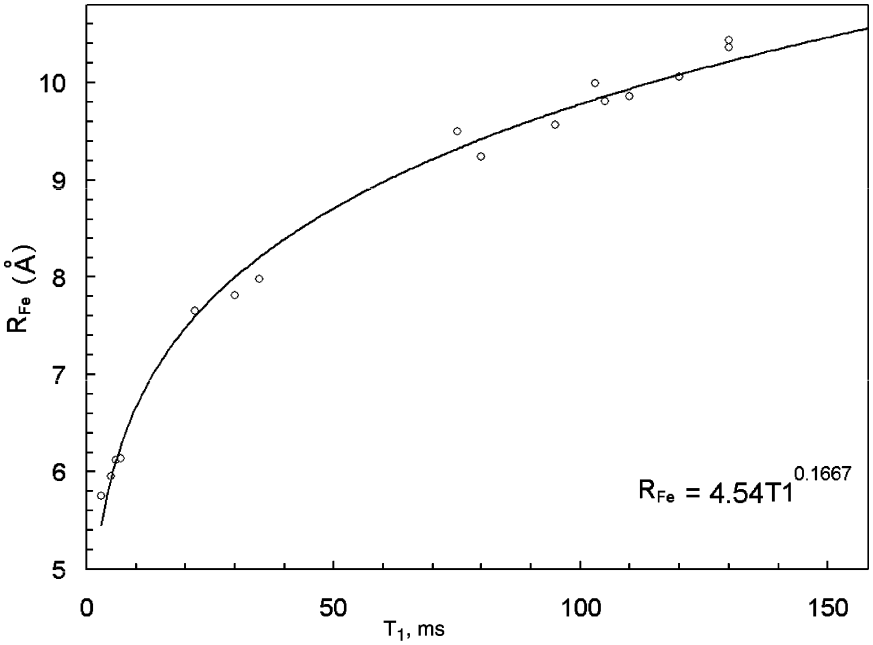

Figure 5. Plot of the expected T_1 (in ms) as a function of distance to the iron, R_{Fe} (in Å), of amino acid residue protons based on the $T_1 \propto R_{Fe}^{-6}$ dependence and the observed $T_1 \sim 6$ ms for a heme methyl ($R_{Fe} = 6^{-1}$ Å), as given by eq 3. The data points correspond to the observed T_1 for assigned protons and the expected R_{Fe} based on the HemO−PH−H_2O crystal structure.[15]

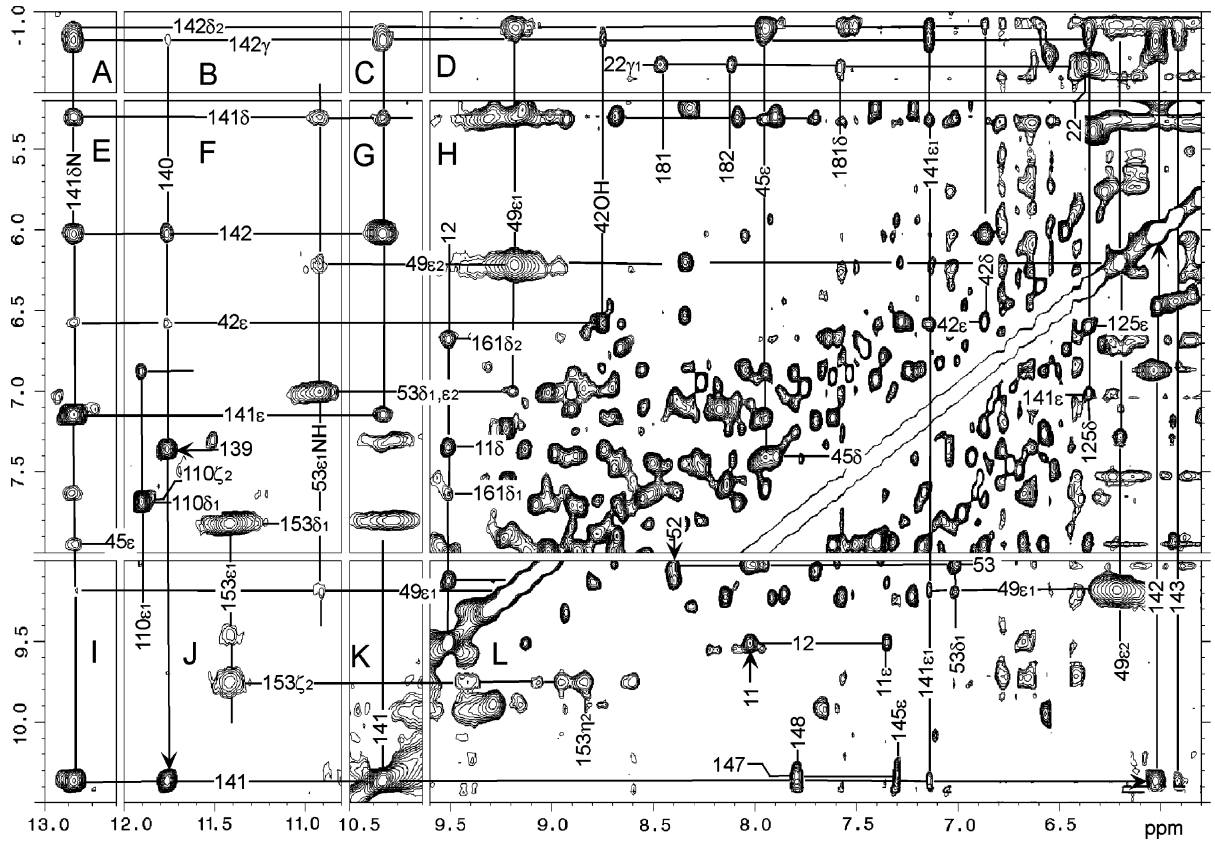

Figure 6. Portion of the low-field NOESY spectrum of HemO−PH−H_2O in ^1H_2O, 50 mM in phosphate at 25 °C, where protons involved in the H-bond network resonate. Illustrates sequential N_i-N_{i+1} connections (shown by arrows) for Ala139-Leu142 (F, H, J, L); the Leu142 contacts with Gln49 NH_2, Tyr42 ring, and OH Phe45 and Phe125 rings (D) as well as to His141 ring (A, D); intra-residue contacts for His141 (E, G, L) and its contacts to Leu142 (D, G), Gln49 NH_2 (I, L), and rings of Phe45 and Tyr42 (A); intra-residue contacts for His53 (F, L) and its contacts with His141 ring (F, L); intra-residue contacts for Gln49 NH_2 (H, L) and its contacts to Leu142 (D), His141 ring (I, L), and His53 (F, H, J). Also shown are the intra-residue contacts for Trp153 (F, J, L) and inter-residue contacts involving the residue pairs Val22/Phe181, Val2122/Ala182 (D), and Ala12/Asn161 (H). Peaks are labeled as given in Figure 3.

ature dependence to the shifts, as well as often weak and/or broad cross-peaks indicative of moderate paramagnetic relaxation for several of the residues. The fragment is described by $Gly_m(N\alpha)_{m+1}$-$(N\alpha)_{m+2}$-AMX_{m+3}-$(N)_{m+4}$-Ala_{m+5}-$(N\alpha)_{m+6}$ (seg-

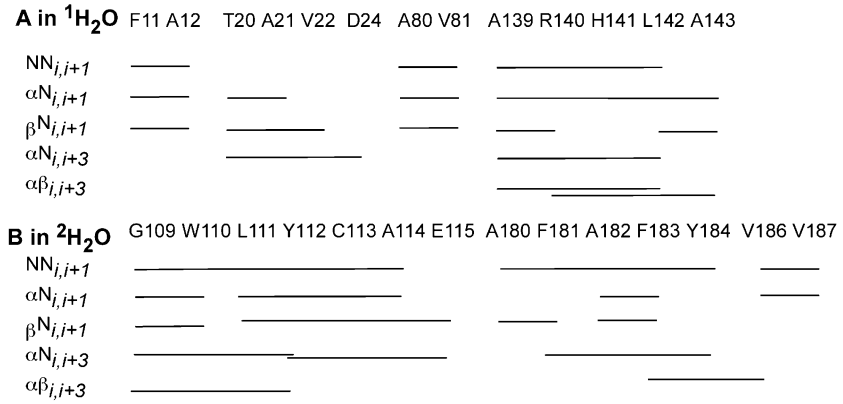

Figure 7. Schematic representation of backbone connectivities for assigned residues of HemO−PH−H_2O in (A) ^1H_2O and (B) ^2H_2O.

ment N_m-N_{m+1} connectivities shown in Figure 8E and 8H) where N_{m+1} and α_{m+1} make contact to a Trp ring and AMX_{m+3} makes contact to a low-field shifted and moderately relaxed two-spin aromatic ring. These data are sufficient to uniquely identify the fragment Gly109-Gln115 and the aromatic rings of Trp110 and Tyr112. The key backbone assignments are illustrated schematically in Figure 7, and chemical shifts are listed in Table 1 and Table S1.

Preliminary Magnetic Axes: The δ_{dip}(obsd) values for the above sequence-specifically assigned residues, used as input for a one-parameter search for the axial anisotropy oriented normal to the heme, lead to $\Delta\chi_{ax} = -2.70 \times 10^{-8}$ m^3/mol. The correlation between δ_{dip}(obsd) and δ_{dip}(calcd) is very good, as shown in Figure 9A, and these preliminary magnetic axes predict (Tables 1 and S1) that at least some protons on four proximal (Thr20 ($C_\gamma H_3$), Val22 (C_γH's), His23 (C_αH), Asp24 (C_βH's)) and five distal (Gly116 (NH), Ser117 (NH, C_αH), Asn118 (C_αH, C_βH's), Gly120 (NH, C_αH's), and Ala121 (C_αH, $C_\beta H_3$) residues would experience sufficiently large δ_{dip}(calcd)* (δ_{dip}(calcd)* designates dipolar shifts generated by the preliminary magnetic axes) to render the resonances resolved either to the low-field of 9 ppm (Gly116, Ser117 NH's) or to the high-field side of 0 ppm (for the other protons with significant δ_{dip}, see Supporting Information). The predicted relaxation for these unassigned, but expected resolved, signals, with R_{Fe} 3.3 to ~9.5 Å, indicates expected T_1's ranging from <1 ms to ~100 ms.

Assignments Based on Crystal Structure and δ_{dip}: We first address the weakly relaxed residues with signals within the diamagnetic envelope. NOESY contacts by Leu142 $C_{\delta 2}H_3$ are predicted to an upfield shifted Phe125 ring, an unshifted Tyr42 ring, and a low-field shifted Phe45 ring, and the relevant cross-peaks (Figure 6D) to TOCSY-detected rings are indeed observed, as are the contacts between the Tyr42 and Phe45 rings (Figure 6D). The ring of the sequence-specifically assigned His141 exhibits NOESY cross-peaks to the Val (not shown) of the Ala-Val pair identified above, uniquely identifying Ala80 and the slightly upfield shifted Val81. A low-field shifted and moderately relaxed Phe ring exhibits strong NOESY cross-peaks to the assigned Ala114 C_αH and $C_\beta H_3$ (Figure 8B, 8H, and 8I) uniquely identifying the Phe52 ring and its backbone. A TOCSY cross-peak (not shown) between a labile proton peak at 11.4 ppm and an aromatic proton with insignificant δ_{dip} at 7.8 ppm (Figure 6J) assign Trp153 $C_{\delta 1}$H, $N_{\epsilon 1}$H. Comparable NOESY cross-peaks of the $N_{\epsilon 1}$H to $C_{\delta 1}$H and a relaxed proton of a low-field shifted three-spin aromatic ring (Figure 6L, Figure 8L) identify three protons of the Trp153 ring; the $H_{\epsilon 3}$ is likely degenerate with $H_{\zeta 3}$. The residue is confirmed by the expected $H_{\eta 2}$ cross-peak to the Tyr112 C_δH and both the moderate paramagnetic relaxation (as indicated by broad, weak cross-peaks) and δ_{dip}(calcd) (Figure 8H). Strong NOESY cross-peaks (Figure 8I) of the Tyr112 C_αH with two protons of a three-spin ring uniquely identify Phe156. NOESY contacts between the assigned Phe11 ring protons and an inconsequential shifted Ala, an upfield shifted NH_2 group (not shown), and an upfield shifted isopropyl identify Ala173, the terminus of Leu15, and the Asn161 NH_2 group. The C_αH of Phe52 (part of a $NHC_\alpha H-C_\beta H_2$ spin system) is identified by its very strong NOESY cross-peak to the Phe183 C_ϵH's, and its NH exhibits a cross-peak to another NH in contact with a His ring CH, assigning the backbone and one ring CH of His53. A low-field shifted $NHC_\alpha H-C_\beta H_2$ fragment with the C_αH at 5.35 ppm fails to exhibit any detectable NOESY cross-peaks. However, only Met31 among the unassigned residue is predicted to exhibit the observed low-field bias (the assignment is confirmed based on NOEs from the heme; see below and Supporting Information). Diagnostic contacts among a series of aromatic rings further identify Phe36 (in contact with Tyr42), Tyr133 in contact with His137, and His145 in contact with His152 (not shown).

Three of the proximal residues with predicted resolved signals are readily assigned with the analyses of relaxation and NOE/NOESY data. Thus an upfield shifted, complete Val exhibits $C_\gamma H_3$ NOESY cross-peaks to the assigned proximal Phe181 backbone to identify Val22 (Figure 4E), and the $C_\beta H_3$ of an upfield shifted, complete Ala exhibits a NOESY cross-peak to the Val22 NH (not shown) to assign it uniquely to Ala21. A CH_3CHCH fragment with resolved and relaxed CH_3 as well as strongly upfield shifted C_αH, exhibits the NOESY cross-peak to Ala21 (not shown) diagnostic for Thr20. Last, the Ala21 C_αH exhibits a strong NOESY cross-peak to one of a relaxed (T_1 ~70 ms, R_{Fe} ~9 Å) pair of strongly spin-coupled (not shown, see Supporting Information Figure S3), partially resolved, protons for which only the Asp24 C_βH's satisfy both the NOE and relaxation constraints. It is noted that once the candidates are identified by δ_{dip}(calcd)* and R_{Fe}, standard backbone NOESY cross-peaks (summarized in Figure 7) provide the confirmation for these assignments.

Four of the five distal helix residues with predicted resolved (Table 1) but strongly relaxed signals are uniquely assigned upon considering δ_{dip}(calcd)*, T_1, crystal coordinates, and confirming NOE/NOESY data. Thus Ala121 is predicted to exhibit strongly upfield shifted (~ −4 ppm) and moderately relaxed (R_{Fe} ~9 Å) $C_\beta H_3$, while the C_αH is even further upfield (−5 ppm) and

Table 1. ^{1}H NMR Data for Key Residues of HemO−PH−H_2O[a]

residue	proton	δ_{DSS}(obsd)[b]	δ_{dip}(obsd)[c]	δ_{dip}(calcd)[d]	δ_{dip}(calcd)[e]	R_{Fe}[f] (T_1)[g]
Thr20	NH	6.02	−1.20	−0.97	−0.92	10.7
	$C_\alpha H$	1.70	−2.96	−2.85	−2.68	8.1
	$C_\beta H$	2.69	−1.20	−1.19	−1.07	10.8
	$C_\gamma H_3$	−0.60	−1.76	−2.05	−1.77	9.4 (100)
Ala21	NH	6.60	−1.10	−1.35	−1.33	11.2
	$C_\alpha H$	2.03	−1.71	−1.68	−1.66	11.1
	$C_\beta H_3$	0.15	−0.71	−0.98	−1.00	
Val22	NH	6.36	−1.11	−1.45	−1.55	10.8
	$C_\alpha H$	2.19	−1.20	−1.39	−1.56	10.8
	$C_\beta H$	0.65	−1.10	−0.83	−0.96	11.8
	$C_{\gamma1} H_3$	−0.63	−0.70	−0.94	−1.13	10.4 (130)
	$C_{\gamma2} H_3$	−0.12	−0.60	−0.71	−0.92	11.2
His23	$C_\alpha H$ (peak c)	−2.8	−5.58	−6.12	−7.28	6.1 (3)
	$C_\beta H$ (peak a)	27.8	h			5.8(2)
Asp24	$C_{\beta1} H$	−0.37	−2.59	−2.52	−2.45	9.2 (80)
	$C_{\beta2} H$	−0.60	−2.57	−2.79	−2.75	9.4
Gln49	$N_{\epsilon1} H$	9.18	i	0.59	0.78	10.3
	$N_{\epsilon2} H$	6.21	i	0.64	1.00	8.7
Phe52	$C_\alpha H$	4.86	0.35	0.36	0.41	13.9
	$C_{\beta1} H$	3.79	0.35	0.44	0.56	11.8
	$C_{\beta2} H$	3.48	0.36	0.57	0.63	
	$C_\delta Hs$	7.76	0.30	0.52	0.63	11.5
	$C_\epsilon Hs$	8.15	0.62	0.76	0.88	10.5
	$C_\zeta H$	8.55	1.00	1.10	1.19	9.8
His53	NH	9.02	0.87	0.15	0.24	
	$C_\alpha H$	4.57	0.34	0.07	0.17	
	$C_{\beta1} H$	3.09	0.11	−0.09	0.00	
	$C_{\beta2} H$	2.77	0.05	−0.03	0.06	
	$C_{\delta1} H$	7.01	−0.23	−0.20	−0.06	
	$C_{\epsilon2} H$	7.06	−0.82	−0.52	−0.21	9.9
	$N_{\delta2} H$	10.92	i	−0.07	0.09	
Tyr112	NH	9.18	0.50	0.52	0.54	
	$C_\alpha H$	5.30	0.57	0.73	0.76	11.1
	$C_{\beta1} H$	4.38	0.97	0.72	0.73	11.7
	$C_{\beta2} H$	4.00	0.88	0.63	0.64	
	$C_\delta Hs$	8.30	0.57	0.96	0.95	10.6
	$C_\epsilon Hs$	8.82	1.06	1.24	1.23	9.3
	$O_\eta H$	15.0	i	1.89	1.97	8.1
Cys113	NH	9.32	0.99	1.02	1.04	10.4 (130)
	$C_{\beta1} H$	4.45	1.27	1.21	1.24	9.9
	$C_{\beta2} H$	3.85	1.20	1.32	1.28	9.5
	$C_{\beta2} H$	3.85	1.20	1.32	1.28	9.5
Gly116	NH (peak b)	9.5	1.22	1.03	1.16	8.0 (35)
Asn118	$C_\alpha H$	−1.66	−5.00	−4.96	−4.76	7.6 (22)
	$C_{\beta1} H$	−0.41	−2.70	−2.25	−2.22	9.7
	$C_{\beta2} H$	−0.26	−2.62	−2.21	−2.16	9.1
Gly120	$C_{\alpha1} H$ (peak d)	−26	−24	−22.50	−29.27	3.5 (<1)
Ala121	$C_\alpha H$	−5.8	−6.30	−6.11	−6.12	6.1 (7)
	$C_\beta H_3$	−3.14	−4.10	−4.66	−4.54	7.8 (30)
Phe123	$C_\delta Hs$	8.82	0.58	1.21	1.18	9.7
	$C_\epsilon Hs$	8.56	0.98	0.86	0.86	11.3
Arg140	NH	11.77	i	−0.28	−0.24	
	$C_\alpha H$	3.46	−0.40	−0.37	−0.35	
	$N_\epsilon H$	9.72	i	−0.19	−0.18	
	$N_{\eta1} H$	6.43	i	−0.23	−0.22	
	$N_{\eta2} H$	6.74	i	−0.15	−0.14	
His141	NH	10.37	i	−0.42	−0.36	
	$C_\alpha H$	3.30	−0.72	−0.62	−0.54	
	$C_{\delta2} H$	5.31	−1.17	−0.83	−0.63	11.2
	$C_{\epsilon1} H$	7.14	0.00	−0.23	−0.14	
	$N_{\delta1} H$	12.88	i	−0.33	−0.26	
Leu142	NH	6.03	−0.57	−0.69	−0.63	
	$C_\alpha H$	2.32	−1.38	−1.54	−1.44	10.8
	$C_{\beta1} H$	0.10	−1.56	−1.14	−1.08	11.1
	$C_{\beta2} H$	0.70	−0.83	−0.74	−0.68	12.7
	$C_\gamma H$	−0.77	−0.60	−0.72	−0.61	11.8 (130)
	$C_{\delta1} H_3$	0.33	−0.98	−0.44	−0.36	12.0
	$C_{\delta2} H_3$	−0.85	−1.02	−1.36	−1.15	9.6 (80)
Trp153	$C_{\delta1} H$	7.82	0.32	0.44	0.33	11.2
	$N_{\epsilon1} H$	11.43	0.89	0.90	0.83	10.4
	$C_{\epsilon3} H$	7.00	0.00	−0.07	−0.15	10.1
	$C\zeta_2 H$	9.76	1.52	1.30	1.28	9.5
	$C_{\zeta3} H$	7.04	0.00	0.49	0.49	9.5
	$C_{\eta2} H$	8.85	1.88	1.28	1.27	9.2

Table 1 (Continued)

residue	proton	δ_{DSS}(obsd)[b]	δ_{dip}(obsd)[c]	δ_{dip}(calcd)[d]	δ_{dip}(calcd)[e]	R_{Fe}[f] (T_1)[g]
Tyr184	NH	9.05	0.86	0.57	0.48	12.0
	$C_\alpha H$	4.86	0.74	0.65	0.62	
	$C_{\beta 1} H$	4.40	1.21	0.96	0.78	9.9
	$C_{\beta 2} H$	4.18	1.40	1.09	1.00	10.1
	$C_\delta H$	7.6	0.68	1.13	1.06	10.8
	$C_\epsilon Hs$	8.1	1.01	1.29	1.33	9.4
Pro206	$C_{\gamma 1} H$	1.90	−1.50	−1.75	−1.62	8.7
	$C_{\gamma 2} H$	1.31	−2.20	−1.93	−1.65	8.6
	$C_{\delta 2} H$	2.73	−0.56	−0.97	−0.89	11.1

[a] HemO−PH−H_2O in ^1H_2O, 100 mM in phosphate, pH 7.0 at 25 °C. [b] Observed chemical shift, in ppm, referenced to DSS. [c] Observed dipolar shift, given by eq 5. [d] Dipolar shift determined for preliminary magnetic axes (Figure 9A), with $\alpha = 0$, $\beta = 0$, and $\Delta\chi_{ax} = -2.7 \times 10^{-8}$ m^3/mol, using only sequence-specifically assigned residues. [e] Dipolar shift determined for robust magnetic axes (Figure 9B) resulting from a three-parameter least-squares search with $\alpha = 195°$, $\beta = 5°$, and $\Delta\chi_{ax} = (-2.62 \pm 0.05) \times 10^{-8}$ m^3/mol. [f] Distance between proton and iron, in Å, as determined from the crystal structure of HemO−PH−H_2O,[15] for protons ≤12 Å (T_1 < 250 ms) from the iron. [g] T_1 values, in ms, determined from null in inversion−recovery T_1 experiment. [h] The axial His $C_\beta H$ hyperfine shift is dominated by the contact shift. [i] No reliable estimate to diamagnetic reference due to strong, and likely variable, H-bonding.

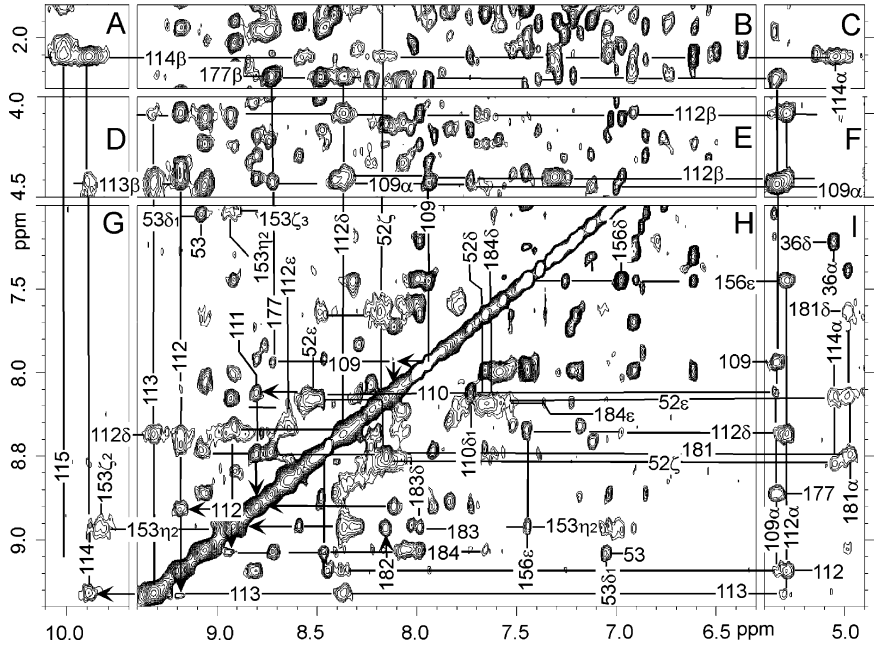

Figure 8. Portion of the low-field NOESY spectra of HemO−PH−H_2O 4 weeks after converting from ^1H_2O to ^2H_2O solution, 50 mM in phosphate, pH 7.0 and 23 °C. Illustrated are sequential N_i−N_{i+1} contacts (shown by arrows) for residues Gly109-Ala114 (H) and α_i-N_{i+1}-β_i-N_{i+} key contacts for residue pairs A114β/E115 (A), Y112α/C113N (I), and C113β/A114 (D). The intra-residue cross-peaks are shown for G109 (E), Y112 (E, F, H), A114 (A, C), and the rings of Phe52, Phe83, Phe156, and two-spin residue X and two-spin aromatic residue Y (H), as well as part of the Trp153 ring (G, H). Key cross-peaks are also shown for the residue pairs W153/F156 (H) and F52/A114 (B, I). Peaks are labeled as given in Figure 3.

should exhibit stronger relaxation (R_{Fe} ~5.0 Å). Such signals are indeed observed, with $C_\alpha H$ to $C_\beta H_3$ NOE only observed by 1D NOEs (not shown), but the expected Ala121 $C_\beta H_3$ NOESY contacts to Leu142 $C_{\delta 2} H_3$ and $C_\alpha H$ are clearly observed in Figure 4D. Both the δ_{dip} and T_1's are very well predicted (Figures 5 and 9A). A moderate NOESY cross-peak (not shown) for Ala121 $C_\beta H_3$'s to a strongly relaxed (T_1 ~15 ms, R_{Fe} ~7.5 Å) single proton peak at −1.8 ppm is that predicted solely for Ala118 $C_\alpha H$ by the δ_{dip}(calcd)*, R_{Fe}, and crystal structure. In turn, the Asp118$C_\alpha H$ exhibits strong NOESY cross-peaks to an upfield shifted, weakly relaxed pair of spin-coupled protons near −0.3 ppm (Figure 4F), identifying the Asn118 $C_\beta H$'s by both relaxation and δ_{dip}(calcd)*, and to the Glu115 $C_\alpha H$ (not shown), as expected. Strong NOESY cross-peaks between the Asn118 $C_\beta H$'s to a pair of very strongly dipolar coupled labile protons, (not shown; see Supporting Information) lead to the identification of the Arg77 NηH_2 group.

Both Ser117 and Gly116 predict NH shifts (δ_{dip} 1−2 ppm) in the 9.5 ppm range. However, peak b (Figure 3C) exhibits T_1 ~20 ms, which is consistent with R_{Fe} ~8.0 Å for Gly116 but completely inconsistent with R_{Fe} 3.7 Å for Ser117. Ser117 $C_\alpha H$ and Gly120 $C_{\alpha 2} H$ are predicted to resonate in the −1 to −5 ppm window (see Supporting Information), but their expected severe relaxation (R_{Fe} 3.7 Å, T_1 >1 ms, R_{Fe} 5.3 Å, T_1 ~3 ms, respectively) would render such extremely broad peaks undetectable among the numerous less severely relaxed proton signals in this spectral window. The $C_\alpha H$ of Ser117 is predicted to resonate (see Table S1) near the −10 to −15 ppm window, but its extreme relaxation (R_{Fe} 3.7 Å) would leave such a peak undetected among the less severely relaxed vinyl H_β's (Figure 2). The $C_{\alpha 2} H$ of Gly120 is predicted (see Table S1) to resonate in the −20 to −25 ppm window, although this peak is also expected to be extremely broad (R_{Fe} ~ 3.5 Å). Nonetheless, this spectral window contains no other hyperfine shifted peaks, and a peak (peak d in Figure 2) has the shift and relaxation consistent with this assignment. The His23 $C_\alpha H$, whose contact shift contribution is expected to be negligible, is the only remaining proton with δ_{dip}(calcd)* (see Table 1) so as to yield

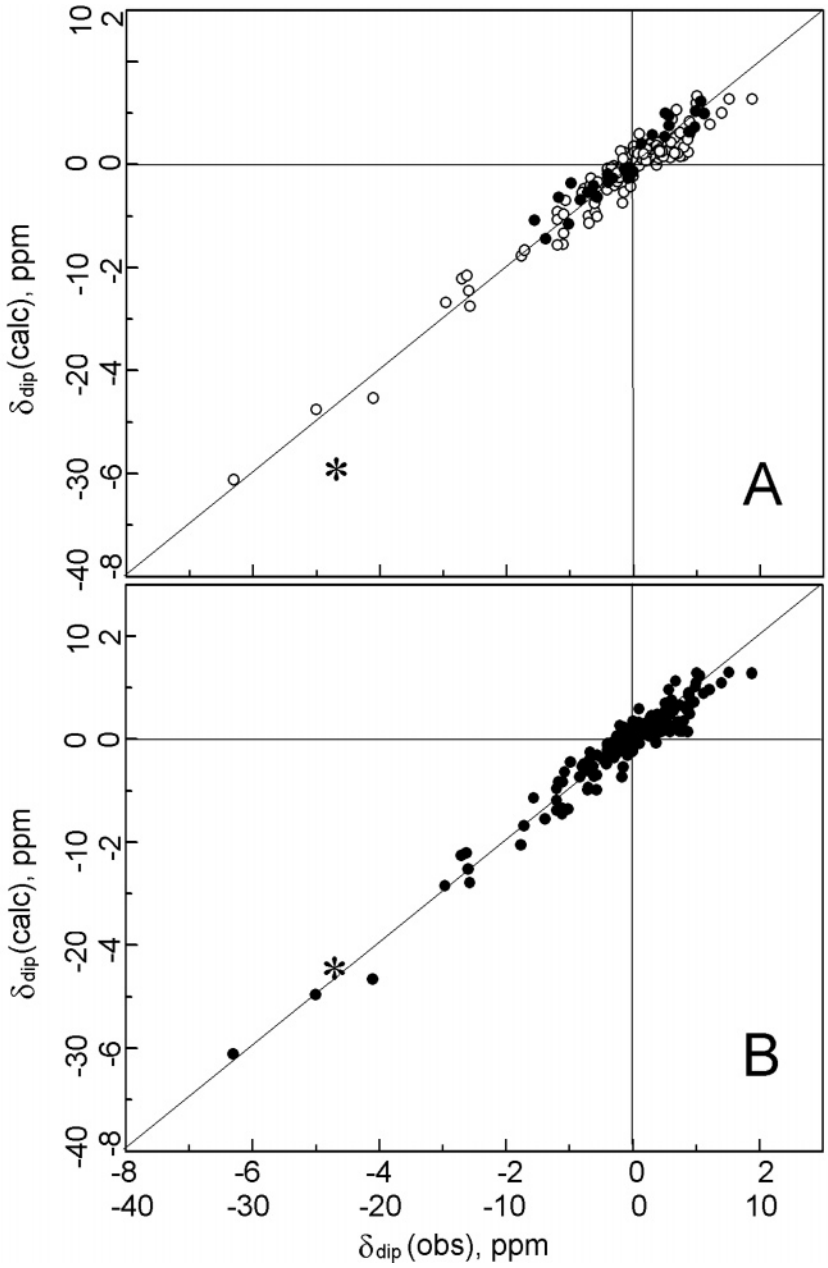

Figure 9. Plot of δ_{dip}(calcd) versus δ_{dip}(obsd) for HemO−PH−H_2O based on NMR data (A) only for sequence specifically assigned residues 9−15 Å from the iron used in a one-parameter search for $\Delta\chi_{ax}$ normal to the heme ($\beta = 0$, $\Delta\chi_{rh} = 0$), with $\Delta\chi_{ax} = -2.70 \times 10^{-8}$ m^3/mol; and (B) all assigned residues used in a three-parameter search for an axial anisotropy ($\Delta\chi_{rh} = 0$), $\Delta\chi_{ax} = -2.67 \times 10^{-8}$, tilted ~5° ($\beta = 5°$) and in a direction toward pyrrole *D* ($\alpha = 210°$). The solid markers indicate data used as input to determine the magnetic axes; open markers and the asterisk indicate the predicted δ_{dip} for assigned residues not used as input. The "inside" scale −8 to +3 ppm applies to the open and closed circles, while the "outside" scale of −40 to +15 ppm applies to the asterisk (Gly120 $C_{\alpha 1}H$).

a resolved, detectable signal, and both the relaxation and chemical shifts of peak d (Figure 4A) are consistent with predictions.

Orientation of Gln49 and His53 Side Chain: These two side chains are involved in the H-bond network that position the proposed catalytic water molecules in the distal pocket of HemO−PH−H_2O. The Gln49 $N_\epsilon H$'s in the crystallographic orientation[19] are expected to exhibit only very weak NOESY cross-peaks to either Leu142 or Val81. A very intense NOESY cross-peak (intensity similar to that of other geminal proton pairs) with no TOCSY connection is observed between two labile protons at 9.2 and 6.2 ppm (Figure 6H). One exhibits a very strong, and the other one a weak cross-peak to Leu142 $C_{\delta 2}H_3$ (Figure 6D) and the ring of His53 (Figure 6H,L). The only possible candidate for this NH_2 group in this vicinity is the Gln49 CO(NH_2), but *only if the Gln49 side chain terminus is rotated 180° about the* $\beta-\gamma$ *bond*, relative to that in the crystal. In this modified orientation, the NH_2 group accounts for all of the observed NOEs.

The NOESY cross-peak patterns of the His53 ring protons to the His141 ring (Figure 6L), Leu142 $C_{\delta 2}H_3$ (Figure 6D) (not shown), Val81 methyls, and (180° rotated) Gln49 NH_2 are not consistent with the crystallographic identification of the $\delta 1$ and $\epsilon 2$ positions as occupied by nitrogens. In fact, the expected unique $\delta 1$ position NOESY cross-peak to the His53 peptide NH is observed for the nonlabile $C_{\delta 1}H$ peak at 7.3 ppm, dictating that nitrogens reside at positions $\delta 2$ and $\epsilon 1$ or that the His53 *side chain ring in solution is rotated 180° about the* $\beta-\gamma$ *bond*

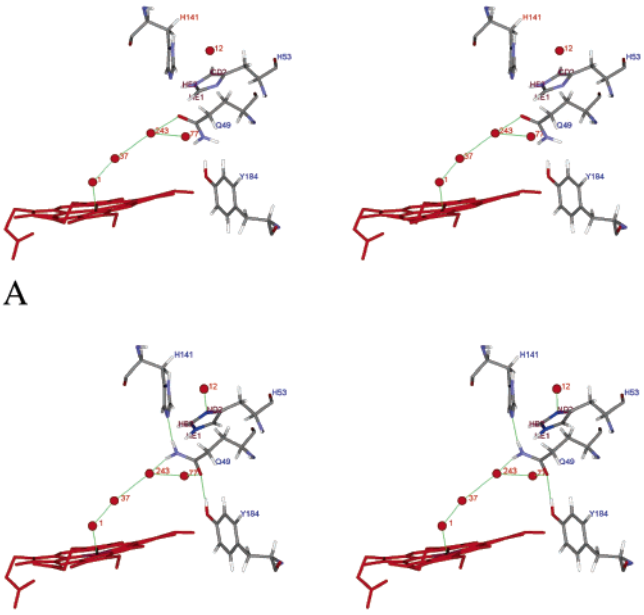

Figure 10. Stereoview of the distal residues Gln49, His53, His141, and Tyr184 and their likely H-bond roles involving the ligated water and the three proposed nonligated catalytically relevant water molecules as (A) depicted in the crystal structure of HemO−PH−H_2O[19] and (B) as determined by ^{1}H NMR based on the 180° rotation about the $\beta-\gamma$ bonds for the side chains of Gln49 and His53. The arrangement indicates expected H-bonds based on X−H···Y $r_{xy} \sim 3$ Å. The geometry of the H-bonds is described in Table 2.

relative to that described in the crystal.[19] The ring labile proton at 10.9 ppm, with its strong NOESY cross-peak to 6.9 ppm (Figure 6G), locates the proton at position ϵ1. The inability to detect a TOCSY cross-peak for the $C_{\delta 1}H$ to the $C_{\epsilon 2}H$, together with the observation of NOESY cross-peaks between the ring CH at 7.3 ppm and the Ala114 $C_\beta H_3$, dictates that the His53 $C_{\delta 1}H$ and $C_{\epsilon 2}H$ are essentially degenerate (and due to dipolar shifts, predicted to be nearly degenerate). The orientation of these two residues, together with two additional side chains in their vicinity, His141 and Tyr184, in the crystal and in solution is compared in Figure 10.

Heme and His23 Assignments: T_1 values and steady-state NOEs among heme substituents and between heme substituents and heme[45] (not shown; details are presented in Supporting Information) yield the unique assignments (and chemical shifts in ppm at 25°), 1-CH_3 (70.0), 3-CH_3 (64.8), 5-CH_3 (76.3), 8-CH_3 (81.2), $2H_{\beta c}$ (−4.0), $2H_{\beta t}$ (11.3), $4H_{\beta c}$ (−8.2), $4H_{\beta t}$ (−15.1), and $6H_\alpha$ (48.2). Five of the remaining six single proton resonances are unassigned but exhibit $T_1 \sim 4$ ms consistent with arising from the other $6H_\alpha$, $7H_\alpha$s, $2H_\alpha$, and $4H_\alpha$. The shorter $T_1 \sim 2$ ms for peak a at 27.8 ppm in Figure 2 is indicative of an axial His23 $C_\beta H$, as observed for other high-spin ferric hemoproteins.[38] Contact of the $4H_\beta$s with a two-spin, low-field shifted aromatic ring assigns it to Tyr184, and a 1-CH_3 NOE to the $C_\alpha H$ of a low-field shifted $C_\alpha HC_\beta H_3$ fragment identifies it as arising from Met31.[32]

Magnetic Axes and Magnetic Properties: The magnetic axes were redetermined using all assigned residues with hyperfine shifts based on a five-parameter search for both anisotropies and the three Euler angles.[38,49] However, while $\Delta\chi_{ax}$, α, and β remained remarkably reproducible with varied input data, the rhombic anisotropy varied in both *sign* and *magnitude*, but never exceeded $|0.1\ \Delta\chi_{ax}|$ with a comparable uncertainty, and the residual error function, $F/n \sim 0.05$ (eq 4), was inconsequentially smaller for a five-parameter (not shown), than that obtained for a three-parameter search for $\Delta\chi_{ax}$, α, and β. Hence our analysis yields $\Delta\chi_{rh} \sim 0$, $\Delta\chi_{ax} = (-2.52 \pm 0.07) \times 10^{-8}$ m^3/mol, $\alpha = 210 \pm 7°$, and $\beta = 7 \pm 1°$, with a good correlation between δ_{dip}(calcd) and δ_{dip}(obsd), as shown in Figure 9B. The orientation of $\Delta\chi_{ax}$ is close to normal to the heme, with a ∼5° tilt relative to the mean N_4−Fe plane and in the approximate direction of pyrrole A. However, inspection of the crystal structure shows[19] that the axial His23 is not oriented perfectly normal to the N_4−Fe plane, but the Fe−N_ϵ-(His23) vector makes a ∼6° angle with respect to the N_4−Fe normal (z') and in the approximate direction of pyrrole D. Hence χ is axial and oriented precisely along the Fe−N_ϵ(His23) vector. Plots of δ_{DSS}(obsd) versus T^{-1} (Curie plot) or T^{-2} exhibited intercepts at $T \rightarrow \infty$ that reproduced the expected δ_{DSS}(dia) only for the T^{-2} plot (not shown), dictating that the dipolar shifts and magnetic anisotropy arise predominantly from the zero-field splitting. This is most clearly manifested for $C_\beta H_3$ of the upfield shifted Ala121 in an intercept at $T = \infty$ of 2.6 ± 0.8 ppm for the T^{-2}, and 8.4 ± 1.0 ppm for the T^{-1} plot (not shown). The determined $\Delta\chi_{ax} = (-2.52 \pm 0.07) \times 10^{-8}$ m^3/mol translates to $D = 9.1 \pm 0.3$ cm^{-1} via eq 2.

Discussion

Structural Characterization: The marginal paramagnetic relaxation at $R_{Fe} > 10$ Å ($T_1 > 100$ ms) permits simple, sequence-specific assignments in ^1H_2O based on NOESY backbone connectivities among TOCSY-detected fragments in a manner similar to that achieved for the low-spin cyanide complex[32] (Figure 6A). Thus, the assignment of the fragment, Ala139−Ala143, that provides two of the strongest H-bond donors is effected, relying only upon the HemO sequence because of the significant low-field bias of NH's due to strong H-bonds.[32,66] The presence of numerous broadened/relaxed NH's and aromatic ring protons in the crowded 6−10 ppm window in ^1H_2O results in resolution problems for additional sequence-specific assignment in ^1H_2O. Thus, the insignificantly relaxed fragment Ala180−Phe183, Val186 Val187 and the moderately relaxed Tyr184 backbone are, in part, resolved in ^1H_2O but can be definitively characterized only in ^2H_2O (Figure 9). For the portion of the distal helix Trp110 through the peptide NH of Gln115, three of the NH's and several $C_\alpha H$'s exhibit moderate paramagnetic relaxation such that their definitive assignments are possible only because of the very slow NH exchange rates to allow detection in ^2H_2O.

For protons with $9 < R_{Fe} < 10$, both TOCSY and NOESY cross-peaks were detected with more rapid repetition of 2D experiments and with shorter mixing times. At $R_{Fe} < 9$ Å, only NOESY cross-peaks could be observed and with $R_{Fe} < 8$ Å, only when the resonance is resolved. Nevertheless, the contribution of primarily the δ_{dip}(calcd)* provided by the preliminary magnetic axes, as well as the T_1 estimate provided by the crystallographic R_{Fe}, and appropriately tailored NOE/NOESY data, it was possible to make extensive assignments that include at least a portion of all but five (Val26, Glu27, Ser117, Leu119, Ala122) of the active site residues with protons with $R_{Fe} < 8$

(66) Wagner, G.; Pardi, A.; Wüthrich, K. *J. Am. Chem. Soc.* **1983**, *105*, 5948−5949.

Table 2. Influence of the Gln49 and His53 Side Chain Orientations on H-Bond Interactions with Other Residues and Ordered Water Molecules

donor	acceptor	r(X···Y)[b]	∠XH···Y[c]
	Crystal Orientation[a]		
His141 $N_{\delta 1}H$	Asp84 CO^{-2}	2.8	~160
Gln49 $N_{\epsilon 2}H$	water #77	2.8	~140
Gln49 $N_{\epsilon 1}H$	Tyr184 O_{η}	2.8	~95
Water #243	Gln49 O_{ϵ}	2.9	
His53 $N_{\delta}H$	Gln49 C═O	3.2	~140
	NMR Orientation[d]		
His141 $N_{\delta 1}H$	Asp84 CO^{-2}	2.8	~160
Gln49 $N_{\epsilon 1}H$	His141 N_{ϵ}	2.8	~160
Gln49 $N_{\epsilon 2}H$	water #243	2.9	~170
His53 $N_{\epsilon 1}H$	Water #77	3.4	~130
Tyr184 $O_{\eta}H$	Gln49 O_{ϵ}	2.8	~180
water #77	Gln49 O_{ϵ}	2.7	
water #12	His53 Nδ2	2.7	

[a] Taken from ref 19; structure depicted in Figure 10A. [b] Distance, in Å, between heteroatom of donor XH and heteroatom acceptor Y. [c] Angle, in degrees, between X−H and H−Y vectors. [d] Solution structure depicted in Figure 10B.

Å. For all but four signals (peaks a, b, c, and d), where δ_{dip} and T_1 guided a potential assignment, it was subsequently possible to detect the crucial NOESY/NOE contact to confirm the assignment. The very good correlation of T_1 with R_{Fe} and δ_{dip}(calcd) with δ_{dip}(obsd) is apparent in Figures 5 and 9, respectively. A sufficient number of heme contact residues were characterized to allow definitive assignment of the heme methyl and vinyl signals without resorting to isotope labeling (not shown; see Supporting Information). The present results bode well for the prospects of homonuclear solution NMR investigations of the physiologically relevant high-spin ferric substrate complex of both point mutants of HemO and other genetic variants of HO.

The NOESY pattern and dipolar shifts confirm an ambient temperature solution structure near the active site that is unchanged from that in crystal structure determined at cryogenic temperature,[19] with two important exceptions involving the side chains of Gln49 and His53. Both residues in solution are found with the side chains reoriented 180° about the $\beta-\gamma$ bond relative to those reported in either the HemO−PH−H_2O or HemO−PH−NO crystal structures (see Figure 10).[19,20] Whether this difference reflects a solution versus crystal, an ambient versus cryogenic temperature structure, or simply an ambiguity of the crystallographic interpretation that renders differentiation of N versus C in the His ring, and C═O versus CNH_2 difficult, is not known at this time. We note that this same 180° rotation of both Gln49 and His53 relative to either crystal structures was observed in solution for HemO−PH−CN.[32] The implication of these side chain reorientations on the distal H-bond network that involves the ordered water molecules is considered below.

Magnetic/Electronic Properties of the Heme: The chemical shift, 82.3, 77.0, 65.0, and 69.0 ppm for the 8-, 5-, 3-, and 1-CH_3, respectively, and their average, 76.2 ppm, are very similar to those of mammalian metMbH_2O complex[38,67] with the isostructural chromophore. The 2-vinyl Hβ (−5.0, −9.6) and 4-vinyl Hβ (−9.0, −11.6) shifts are each larger than that in metMbH_2O[67] and may reflect a more in-plane orientation of the vinyls in HO than Mb environment.

The observed dipolar shifts for nonligated residues were essentially quantitatively reproduced with a paramagnetic susceptibility tensor that is axially symmetric and oriented along the Fe−N_{ϵ}(His23) vector. Similarly dominant axially anisotropic χ_s values have been reported for other high-spin hemoproteins and model compounds.[43−47,51] The magnitude of $\Delta\chi_{ax}$ in high-spin HemO−PH−H_2O is similar to that of the low-spin HO−PH−CN complex,[32] but has the opposite sign. The correlation holds that δ_{dip} for individual residues results in hyperfine shifts in opposite directions in the high-spin and low-spin HO complexes.[32] The dominant T^{-2} dependence for δ_{dip}, and hence $\Delta\chi$, in HemO−PH−H_2O confirms the expected essentially isotropic g values, with the anisotropy arising wholly from zero-field splitting, with $D = 9.1$ cm^{-1}, as previously found for other high-spin ferric heme proteins.[43−45] This value is close to that of metMbH_2O with the isoelectronic chromophore[43,44,46,47] but smaller than values observed for five-coordinate, high-spin, ferric hemoproteins, such as mutant metMb,[51] resting state horseradish peroxidase,[47] and ferricytochromes c′,[45,46] all of which yield larger D values in the range of 12−15 cm^{-1}.

The strong dependence of D on axial field strength (D decreases as axial field strength increases[43]) suggests that the determination of the magnetic axes and through the anisotropy and the T^{-2} dependence of δ_{dip}, D, for high-spin ferric complexes of HO, either for point mutants of HemO or for genetic variants (i.e., hHO or HmuO) should provide significant insight into differences in axial interactions among such complexes.[68] Since the major distal interaction between the ligated water (water #1 in Figure 10) is with one "catalytic", nonligated water molecule identified in the crystal structure,[15,19] variations in D can be interpreted in terms of changes in the distal network of water molecules and the H-bond network.[21,40] While similarly definitive assignments have not yet been achieved for hHO−PH−H_2O or HmuO−PH−H_2O, preliminary results on hHO−PH−H_2O reveal a smaller spread of the resolved, relaxed, and hyperfine shifted signals than that in HemO−PH−H_2O (Zhu, W.; Ortiz de Montellano, P. R.; La Mar, G. N. Unpublished results), suggesting smaller D values and hence somewhat different axial interactions. Similarly, preliminary results on high-spin ferric HemO complexes with chemically modified hemes indicate (Liu, Z.; Yoshida, T.; La Mar, G. N. Unpublished results) that the dipolar shift spread, and hence $\Delta\chi$, D, and axial field strength, responds to perturbations of electronic structure.

Distal H-Bond Network: The crystal structure of HemO−PH−H_2O has identified[19] three nonligated ordered water molecules labeled #37, #77, and #243 (as shown in Figure 10), whose relative positions indicate H-bond interactions between water molecules #37 and #243 and between #243 and #77, with #37 interacting with the ligated water molecule #1. The positions of these three nonligated waters appear largely unchanged upon replacing H_2O with NO in the crystal.[20] The crystallographic orientations of the side chains of Gln49 and His53 are shown in Figure 10A, while their solution orientations are depicted in Figure 10B. The positions of the water molecules and side chain heteroatoms in the crystal indicate[20] that the Gln49 $N_{\epsilon 1}H$ serves as donor to the Tyr184 O_{η}, while the Gln49 $N_{\epsilon}2H$ serves as donor to water molecule #77. The Gln49 C═O_{ϵ} is a position to

(67) La Mar, G. N.; Budd, D. L.; Smith, K. M.; Langry, K. C. *J. Am. Chem. Soc.* **1980**, *102*, 1822−1827.

(68) Caughey, W. S. In *Hemes and Hemoproteins*; Chance, B., Estabrook, R. W., Yonetani, T., Eds.; Academic Press: New York, 1966; pp 276−277.

Table 3. Comparison of H-Bond Strength in HemO−PH−H_2O and HemO−PH−CN

	HemO−PH−H_2O			HemO−PH−CN			
proton	δ_{DSS}(obsd)[a]	δ_{dip}(calcd)[b]	δ^*_{DSS}(dia)[c]	δ_{DSS}(obsd)[d]	δ_{dip}(calcd)[e]	δ^*_{DSS}(dia)[c]	$\Delta\delta^*$[f]
Ala12 NH	9.51	−0.20	9.31	8.96	−0.25	9.21	−0.1
Thr20 NH	6.02	−1.10	7.12	8.37	1.34	7.03	−0.1
Ala21 NH	6.60	−1.33	7.93	9.36	1.49	7.87	−0.0
Val22 NH	6.36	−1.46	7.82	9.44	1.63	7.81	−0.0
Tyr112 NH	9.18	0.49	8.69	8.19	−0.49	8.68	−0.0
Cys113 NH	9.3	0.90	8.40	7.4	−0.79	8.19	−0.2
Ala114 NH	9.9	0.93	8.97	8.04	−0.82	8.86	−0.1
Gly138 NH	10.15	−0.13	10.28	10.43	0.16	10.27	−0.0
Ala139 NH	7.36	−0.22	7.58	7.82	0.26	7.56	−0.0
Arg140 NH	11.77	−0.27	12.04	12.33	0.05	12.28	0.2
His141 NH	10.37	−0.38	10.75	10.91	0.44	10.47	−0.3
Asp147 NH	10.33	−0.25	10.58	11.04	0.22	10.82	0.2
Glu115 NH	10.01	0.70	9.31	9.07	−0.84	9.91	0.6
Gln49 $N_{\epsilon 1}H$	9.18	0.53	8.65	10.14	−0.40	10.54	1. 9
Gln49 $N_{\epsilon 2}H$	6.21	0.61	5.6	7.35	−0.35	7.7	2.1
His53 $N_\epsilon H$	10.92	−0.31	11.23	12.13	0.40	11.73	0.5
Tyr60 $N_\eta H$	9.96	−0.06	10.02	10.43	−0.05	10.48	0.5
Arg140 $N_\epsilon H$	9.72	−0.17	9.89	10.93	−0.06	10.99	1.1
His141 $N_{\delta 1}H$	12.88	−0.71	13.59	13.56	0.85	12.71	−0.9
Trp153 $N_{\epsilon 1}H$	11.43	0.86	10.57	8.69	−1.28	9.97	−0.6
Trp110 $N_{\epsilon 1}H$	11.91	0.18	11.73	11.52	−0.10	11.62	−0.1
Tyr112 $N_\eta H$	15	1.32	13.68	11.68	−1.49	13.17	−0.5

[a] Observed chemical shifts, in ppm, referenced to DSS, in ^1H_2O, 100 mM in phosphate, pH 7.0 at 25 °C. [b] Dipolar shifts calculated from magnetic axes with $\Delta\chi_{rh} = -2.67 \times 10^{-8}$ m^3/mol, $\Delta\chi_{rh} = 0$, $\alpha = 195°$, $\beta = 7° \pm 10$. [c] Diamagnetic chemical shift, $\delta^*_{DSS}(dia) = \delta_{DSS}(obsd) - \delta_{dip}(calcd)$.[32] [d] Dipolar shifts of HemO−PH−CN, calculated for published magnetic axes with $\Delta\chi_{rh} = 2.51 \times 10^{-8}$ m^3/mol, $\Delta\chi_{rh} = -0.58 \times 10^{-8}$ m^3/mol, $\alpha = 95°$, $\beta = 20°$, and $\kappa = 90°$.[32] [e] Observed chemical shifts, in ppm, at 25 °C, taken from ref 32. [f] δ^*_{DSS}(dia; HemO−PH−CN) − δ^*_{DSS}(dia; HemO−PH−H_2O).

act as acceptor to water molecule #243. The His53 ring does not have a heteroatom, from either other residues or water molecules, sufficiently close to form reasonable H-bonds. The His141 ring has the labile proton $N_{\delta 1}H$ as donor to the carboxylate of Asp84, with no apparent donor to interact with $N_\epsilon 2$. The geometric properties of the H-bonds are described[20] in Table 2.

The solution orientations of Gln49 and His53, depicted in Figure 10B, confirm the His141 $N_{\delta 1}H$ H-bond to Asp84, but have the Gln49 $N_\epsilon H$ act as donor to His141 $N_\epsilon 2$, as well as to water molecule #243. Water molecule #77 is now in position to simultaneously serve as acceptor to the His53 $N_{\epsilon 1}H$ and donor to the Gln49 C═O_ϵ. Here, the Gln49 C═O_ϵ is acceptor to the Tyr184 $O_\eta H$. Last, the 180° reorientation of the His53 ring now allows a robust $N_{\delta 2}H$ H-bond to water molecule #12. The geometric properties of the H-bonds in solution are compared to those in the crystal in Table 2. The orientations found in solution clearly allow more effective H-bond stabilization of both the four side chains of interest and two of the three "catalytic" water molecules. It is expected that the solution NMR determined Gln49 and His53 side chain orientations are retained in the O_2 complex, in which case these Gln49 and His53 orientations would favor stronger H-bond donation to the O_2 (and hence proton donation to the nascent Fe−O_2^-) than with the orientations described in the crystal structures.[19,20]

The low-field bias of labile protons, X−H···Y, has been shown to correlate with heteroatom X−Y separation,[66] and this separation correlates with H-bond strength.[69,70] Comparison of H-bond strength in HemO−PH−H_2O and HemO−PH−CN, however, requires correcting the δ_{DSS}(obsd) for the dipolar shift, which is given by

$$\delta^*_{DSS}(dia) = \delta_{DSS}(obsd) - \delta_{dip}(calcd) \qquad (6)$$

where δ_{dip}(calcd) is obtained through the magnetic axes for the respective complexes.[32] Values of δ^*_{DSS}(dia) for labile protons with significant low-field bias, and hence participants in stronger than usual H-bonds, for HemO−PH−H_2O and HemO−PH−CN are compared in Table 3. It is noted that while numerous proximal and distal helix NH's exhibit very different shifts (first 12 entries in Table 3), correction for the respective δ_{dip}(calcd) for the two complexes leads to essentially indistinguishable chemical shifts (difference ≤ |0.2| ppm), and hence inconsequentially altered H-bond strength. Moreover, many of the other labile protons also exhibit very similar shifts. There are, however, several cases where the difference in δ^*_{DSS}(dia) indicates significant alterations in H-bonding strength. We consider only the cases where $\Delta\delta^*_{DSS}(dia) > |0.5|$ ppm, which fall into several distinct regions of the complex. Notable differences in δ^*_{DSS}(dia) are observed in the two complexes for the side chains of Gln49 and His53. The larger low-field bias, and hence stronger H-bonding, for both side chains with CN^- than with H_2O as ligand is consistent with the role of these side chains serving as H-bond donors to water molecules, such that the H-bond donations are stronger when water molecule #37 is a donor to the acceptor ligand CN^- instead of an acceptor to the donor ligand H_2O. The stronger H-bond strength of the His141 $N_{\delta 1}H$ to Asp84 carboxylate H-bond in the HemO−PH−CN and HemO−PH−H_2O complexes is rationalized by stronger donation by the Gln49 $N_{\epsilon 1}H$ to the His141 $N_\epsilon 2$ when there is an H-bond donor rather than acceptor ligand.

Perturbation and H-bonding are also observed for the residues Tyr60 and Glu115 NH. In the crystal, Tyr60 OH and Asn118 $N_\epsilon H_2$ are H-bond donors to the Glu115 carboxylate in HemO−PH−H_2O, but Asn118 NH_2 is reoriented, and Arg77 rotates to serve as donor in HemO−PH−NO.[20] The ^1H NMR data indicate that the rearrangement following ligation of a H-bond acceptor ligand slightly strengthens the Tyr60 $O_\eta H$ and Glu115 NH

(69) Jeffrey, G. A. *An Introduction to Hydrogen Bonding*; Oxford University Press: New York, 1997.
(70) Harris, T. K.; Mildvan, A. S. *Proteins: Struct., Funct., Genet.* **1999**, *35*, 275−282.

H-bonds. The Arg140 $N_\epsilon H$ also exhibits a stronger H-bond in the CN^- complex (Table 3). In the HemO−PH−H_2O crystal structure,[19] the Arg140 side chain is extended away from the distal helix, but is oriented toward and forms an H-bond to Asp81 CO_2^- in the HemO−PH−NO structure.[20] Solution ^1H NMR shows that the Arg140 side chain is oriented toward the distal helix even in the high-spin complex, although an equilibrium between the alternate orientation cannot be discounted. The weaker Arg140 $N_\epsilon H$ H-bond in the H_2O complex is consistent with such an equilibrium favoring the extended Arg140 side chain in the H_2O complex. Last, the Tyr112 $N_\epsilon H$ exhibits a significant change in shift, indicating a stronger H-bond donation to the 6-propionate carboxylate in the H_2O than that in the CN^- complex. This perturbation likely results from the observation that while both propionate carboxylates are oriented toward the proximal side in HemO−PH−H_2O, the 7-propionate carboxylate reorients toward the distal side in both the NO[20] and CN^- [32] complexes.

Dynamic Stability of the Distal Helix: The current model for heme oxygenase function presumes a distal helix that is kinked at the characteristic Gly-Gly (or Gly-Ala) hinge that contacts the heme and is very flexible, as supported by variable location of the distal helix in nonequivalent molecules in the unit cell and relatively large backbone thermal ellipsoids that reflect disorder/dynamics.[15,16,71] The present data on HemO, however, show that at least the N-terminal portion of the distal helix exhibits remarkable dynamic stability, as reflected in the very long lifetimes for NH exchange (half-lives > 1 month). Two other helices exhibit similarly slow exchange, proximal helix H (including Ala180-Val187) that makes contact with the heme, and part of helix 8 that contains the Phe52-His53. It has been noted previously that residues on the N-terminal position of the distal helix exhibit NH peak intensity for ∼24 h after dissolution in ^2H_2O,[32] suggesting that a dynamically very stable part of the distal helix may be crucial to effective catalysis. The generality of this distal helix stability is under current study.

Acknowledgment. This research was supported by a grant from the National Institutes of Health, GM 62830 (GNL), and by grants-in-aid from the Ministry of Education, Science, Sports, and Culture, Japan #14580641 (T.Y.).

Supporting Information Available: One table (^1H NMR spectral data for all assigned residues) and five figures (TOCSY spectra for aromatic rings, aliphatic side chains, key backbone connections, steady-state NOEs for heme resonance assignments, and upfield Asn118/Asp24 NOESY connectivities. This material is available free of charge via the Internet at http://pubs.acs.org.

JA042339H

(71) Lad, L.; Schuller, D. J.; Shimizu, H.; Friedman, J.; Li, H.; Ortiz de Montellano, P. R.; Poulos, T. L. *J. Biol. Chem.* **2003**, *278*, 7834−7843.